Lattice crossover and phase transitions in $NdAlO_3$–$GdAlO_3$ system

L. Vasylechko [a*], H. Shmanko [a], N. Ohon [a], Yu. Prots [b], S. Hoffmann [b], S. Ubizskii [a]

[a] Lviv Polytechnic National University, 12 Bandera St., 79013 Lviv, Ukraine

[b] Max-Planck-Institut für Chemische Physik fester Stoffe, Nöthnitzer Strasse 40, 01187 Dresden, Germany

[*] Corresponding author:
Semiconductor Electronics Dept.
Lviv Polytechnic National University,
12 Bandera St.,
79013 Lviv
Ukraine

Phone: +38-032-2582696
Fax: +38-032-2375089
E-mail: crystal-lov@polynet.lviv.ua

Abstract

Phase and structural behaviour in the (1-x)$NdAlO_3$–$xGdAlO_3$ system in a whole concentration range has been studied by means of *in situ* high-resolution X-ray synchrotron powder diffraction technique and differential thermal analysis. Two kinds of solid solutions $Nd_{1-x}Gd_xAlO_3$ have been found at room temperature: one with rhombohedral ($x < 0.15$) and one with orthorhombic ($x \geq 0.20$) symmetry. A morphotropic phase transition occurs at $x \approx 0.15$, where the co-existence of both phases was observed. Peculiarity of the orthorhombic solid solution is the lattice parameter crossover at the compositions with x = 0.33, 0.49 and 0.62. First-order structural transition $Pbnm \leftrightarrow R\bar{3}c$ has been detected both from *in situ* powder diffraction and thermal analysis data. Continuous phase transformation $R\bar{3}c \leftrightarrow Pm\bar{3}m$ above 2140 K has been predicted for Nd-rich sample $Nd_{0.85}Gd_{0.15}AlO_3$ from the extrapolation of high-temperature behaviour of the lattice parameter ratio of the rhombohedral phase. Based on the experimental data, the phase diagram of the pseudo-binary system $NdAlO_3$–$GdAlO_3$ has been constructed.

Key words: mixed rare earth aluminates; perovskite; solid solution; crystal structure; phase transition; phase diagram

1. Introduction

Mixed oxides in the R_2O_3–Al_2O_3 systems (R = rare earth element) are promising materials for diverse optical, electronic, structural, and magnetic applications. For instance, it has been demonstrated that single crystals of pure and doped $RAlO_3$ perovskites can be used as substrates for the epitaxial growth of thin films of high-temperature superconductors, ferroelectrics, and colossal magnetoresistance oxides, as host for laser active ions and as scintillators. $RAlO_3$ aluminates and solid solutions based on them are used as microwave dielectric materials and as materials for solid oxide fuel cells. For example, $NdAlO_3$–$CaTiO_3$ ceramics are attractive candidates for use as dielectric resonators in wireless communication systems [1–3], whereas $Gd_{1-x}Ca_xAlO_{3-\delta}$ was recently proposed as a fast ion conductor [4]. Rare earth doped gadolinium aluminate $GdAlO_3$:R (R = Ce, Eu, Tb, Dy, Er, Yb) is a promising material for an application as phosphors and scintillators [5–9], because it exhibits high density, chemical and thermal stability, and unique electronic and spectroscopic properties. Moreover, $GdAlO_3$ based materials have also potential application as regenerator material for sub-4K cryocoolers [10], shows promising opportunities for high-temperature applications in gas turbine engines [11–13] and are currently under development as candidate materials for the neutron absorption and control rod applications [14].

The useful physical and chemical properties of the systems based on rare earth aluminates are closely linked to their variable phase composition and crystallography. The crystal structure itself can be easily influenced either by iso/aliovalent substitutions in both anion and cation sites or by varying temperature and/or pressure [15]. Therefore, they are ideal model systems to study structure-property relations. The knowledge of the crystal structure and the resulting physical properties opens up pathways for tailoring of perovskite properties by manipulating their structures. Thus, by modifying the crystal structure of perovskites, their physical and physico-chemical properties can be tuned until a material with the desired properties is obtained.

In continuation of our systematic studies [15] we focused on the system (1-x)$NdAlO_3$–$x$$GdAlO_3$. At room temperature, the end members of the system – $NdAlO_3$ and $GdAlO_3$ – adopt two different variants of the distorted perovskite structure: rhombohedral ($NdAlO_3$ structure type, space group $R\bar{3}c$), and orthorhombic ($GdFeO_3$ structure type, space group *Pbnm*), respectively [15–16]. Both compounds undergo structural phase transitions at elevated temperatures. $NdAlO_3$ transforms continuously from the rhombohedral to a cubic perovskite structure (space group $Pm\bar{3}m$) within the temperature range of 1373–2180 K [17–21], whereas $GdAlO_3$ undergoes a first-order phase transition from the orthorhombic to a rhombohedral crystal structure at 1973 K [19, 22–23]. The great discrepancy in the transition temperature for $NdAlO_3$ may be explained by difficulties in the detection of the continuous phase transition by using of low resolution thermal analysis or laboratory X-ray diffraction techniques. From the analysis of numerous data on similar phase transitions in the related $R$$AlO_3$ compounds (R = La, Ce, Pr) and corresponding solid solutions it was concluded that the rhombohedral-to-cubic transition in $NdAlO_3$ occurs around 2100 K [15]. An additional phase transition in $NdAlO_3$ from the rhombohedral to an orthorhombic structure has been predicted at 16 K from the extrapolation of transition temperatures in the $Nd_{1-x}Sm_xAlO_3$ solid solution [24]. This transition, however, was not confirmed using synchrotron powder diffraction data collected *in situ* at temperatures down to 12 K [25] and neutron diffraction measurements at 0.5 and 1 K [26]. High-temperature phase transition in $GdAlO_3$ from an orthorhombic to rhombohedral structure has been detected at 1973 K both by *in situ* X-ray diffraction and differential thermal analysis (DTA) [19]. Besides, from extrapolation of the c/a parameter ratio of the rhombohedral phase, a continuous transition to the cubic phase was predicted near 2580 K, which is however above the melting point (2273 K). The X-ray synchrotron powder diffraction investigations performed *in situ* in the temperature range of 14–1170 K revealed that the $GdAlO_3$ structure remains orthorhombic on cooling down to

14 K [15]. However, clear anomalies in the structural behaviour were detected at low temperatures, which manifest in a very low and sinusoidal (sigmoid) character of thermal expansion in *b*-direction, including negative expansion in the temperature range of 70–210 K [15].

In this work we present the results of the phase and structural characterisation of the pseudo-binary system $NdAlO_3$–$GdAlO_3$ in a broad temperature range by a combination of X-ray phase and structural analysis, *in situ* high-temperature X-ray synchrotron powder diffraction and DTA techniques.

2. Experimental and data analysis

2.1 Synthesis

Series of the $Nd_{1-x}Gd_xAlO_3$ samples with x in the range of 0.1–0.9 were prepared from the oxides Nd_2O_3, Gd_2O_3 and Al_2O_3 according to the following reaction scheme:

$$(1-x)Nd_2O_3 + xGd_2O_3 + Al_2O_3 \rightarrow 2Nd_{1-x}Gd_xAlO_3$$

Appropriate amounts of the previously fired oxides were mixed and pressed to pellets which were subsequently loaded into alumina crucibles and reacted in air at 1300 K for 24 h. In a final synthesis step the sintered pellets were arc-melted in Ar atmosphere.

2.2 Powder X-ray diffraction (PXRD)

X-ray phase and structural characterisation of the samples at room temperature was performed by the laboratory Huber imaging plate Guinier camera G670 (Cu $K_{\alpha 1}$ radiation, λ = 1.54056 Å). The temperature depending investigations of the crystal structure were carried out by the high-resolution powder diffraction technique applying synchrotron radiation at the beamline B2 at HASYLAB/DESY (Hamburg, Germany). The diffraction experiments were performed in Debye-Scherrer capillary vertical geometry at the powder diffractometer equipped with a STOE furnace and on-site readable imaging plate detector OBI [27, 28]. The wavelengths of 0.53824 Å and 0.65125 Å were calibrated using the reflection positions of silicon reference material (NIST SRM 640b). All crystallographic calculations including refinements of the lattice parameters, positional and displacement parameters of atoms were performed by full-profile Rietveld refinement by means of the program package WinCSD [29].

2.3 Thermal analysis

Differential thermal analysis (DTA) was performed on DSC204 and DSC404C thermal analysers (NETZSCH, Selb) in argon atmosphere. High-temperature DTA curves were recorded with a Pt10%Rh-Pt thermocouple (type S) and Al_2O_3 crucibles in the

temperature range from 300 K to 1473 K and with heating rates of 10 and 20 K/min. Transition temperatures were extracted from the onsets of the thermal signal in the heating cycles.

3. Results

3.1 Structural evolution of $Nd_{1-x}Gd_xAlO_3$ at room temperature

PXRD examination at room temperature revealed almost pure perovskite phase for all $Nd_{1-x}Gd_xAlO_3$ specimens. Only in two compositions the minor amount of impurity phases has been detected, namely $Gd_4Al_2O_9$ in the sample with $x = 0.9$ and monoclinic $Nd_{2-x}Gd_xO_3$ in the specimen with $x = 0.15$. The reflection splitting observed for the $Nd_{0.9}Gd_{0.1}AlO_3$ sample indicates the rhombohedral structure similar to $NdAlO_3$. The gadolinium-rich specimens display orthorhombic perovskite structure isotypic with $GdFeO_3$. No detectable reflection splitting was observed for the $Nd_{1-x}Gd_xAlO_3$ samples with the intermediate Nd/Gd ratio; however the presence of weak superstructure reflections points on the $GdFeO_3$ type of structure for these compositions. The refinement of $Nd_{1-x}Gd_xAlO_3$ structures was performed in space groups $R\bar{3}c$ for $x = 0.1$ and *Pbnm* for $x \geq 0.20$. Full-profile Rietveld refinement based on X-ray and synchrotron powder diffraction data showed good fits between experimental and calculated profiles for all compositions (see for example Fig. 1) and led to the final values of the structural parameters and residuals presented in Table 1. For the PXRD pattern of $Nd_{0.85}Gd_{0.15}AlO_3$ specimen, which contains both perovskite phases, simultaneous two-phase Rietveld refinement was performed (Fig. 2 and Table 1).

The dependence of the normalized lattice parameters and unit cell volumes as function of the composition is presented in Fig. 3. The formation of two kinds of solid solutions can be derived from this plot. Both the rhombohedral and orthorhombic phases coexist in the narrow compositional range with $x \approx 0.15$. The unit cell volume of orthorhombic solid solution $Nd_{1-x}Gd_xAlO_3$ decrease almost linearly in accordance with decreasing radii of rare earth cations ($r(Nd^{3+}) = 1.303$ Å, $r(Gd^{3+}) = 1.107$ Å for coordination number 9 after Shannon [30]). However, minor negative deviation from the Vegard's (Zen's) law is observed in the solid solution with rhombohedral crystal structure, which may indicate some degree of short-range ordering of the rare earth cations in the crystal lattice.

Remarkable feature of the $Nd_{1-x}Gd_xAlO_3$ solid solution with orthorhombic crystal structure ($x \geq 0.20$) is the lattice parameter crossover (outlined in Fig. 3), resulting in the appearance of metrically tetragonal and cubic lattices at certain compositions. As a result, four regions of the solid solution with different relations of the lattice parameters are observed in the system, namely, ranges **I** ($a_p > c_p > b_p$), **II** ($a_p > b_p > c_p$), **III** ($b_p > a_p > c_p$) and

IV ($b_p > c_p > a_p$). For certain compositions, the dimensions of the unit cells are very close to tetragonal or cubic; however, the symmetry of these structures remains orthorhombic. This is confirmed by an analysis of concentration dependencies of the selected interatomic distances (Fig. 4), which shows a systematic increase of orthorhombic perovskite deformation in the $Nd_{1-x}Gd_xAlO_3$ series at increasing Gd content [15]. These dependencies also reflect very well the morphotropic phase transition between rhombohedral and orthorhombic structures at x = 0.15, which is manifested in the redistribution of the interatomic distances in the $Nd_{1-x}Gd_xAlO_3$ structures (Fig. 4).

3.2 Temperature evolution of the structure

DTA revealed endothermic effects in the $Nd_{1-x}Gd_xAlO_3$ samples with x = 0.10, 0.15, 0.20, 0.25, 0.30, 0.40, 0.50, 0.60, 0.70 at the temperatures 205, 288, 411, 469, 630, 773, 1053, 1253 and 1453 K, respectively, which points to a first-order phase transformations occurred in these specimens. As examples, the DTA curves of the samples with x = 0.10, 0.15 and 0.25 are presented in Fig. 5. *In situ* high-temperature synchrotron powder diffraction on the selected specimens with x = 0.15, 0.25 and 0.40 confirmed the presence of the structural transitions. The analysis of the diffraction patterns in the vicinities of the transition temperatures revealed coexistence of both low-temperature orthorhombic and high-temperature rhombohedral phases, which proves the 1st-order discontinuous character of the phase transition.

Crystal structure parameters of rhombohedral and orthorhombic modifications of $Nd_{1-x}Gd_xAlO_3$ samples with x = 0.15, 0.25, 0.40 and 0.60 at the elevated temperatures have been refined by full-profile Rietveld method. For the specimens with x = 0.15, 0.25 and 0.40 two-phase Rietveld refinement have been performed in the regions of the phase transitions, which also allowed to estimate the relative amounts of both perovskite phases. According to the data obtained, the contents of the orthorhombic phase in $Nd_{0.75}Gd_{0.25}AlO_3$ sample decreases from 59 wt.% at 473 K to 12 wt.% at 523 K, whereas the content of rhombohedral phase increases respectively. For the $Nd_{0.60}Gd_{0.40}AlO_3$ specimen, the amount of *Pbnm* phase decreases from 80 wt.% at 773 K to 25 wt.% at 873 K.

The thermal evolution of the lattice parameters of the $Nd_{1-x}Gd_xAlO_3$ samples with x = 0.15, 0.25, 0.40 illustrating the 1st-order phase transition from the orthorhombic to rhombohedral structure are presented in Figs. 6*a*–*c*. No structural transition has been detected in $Nd_{0.40}Gd_{0.60}AlO_3$ up to 1173 K, although the lattice parameter crossover observed in orthorhombic phase at 800–1170 K (see Fig. 6*d*) indicates a forthcoming transformation to rhombohedral structure [15]. According to DTA data such transition occurs in this sample at

1257 K. Analysis of temperature evolution of the unit cell parameters and their ratio in rhombohedral perovskites allows to predict the temperature of the continuous transformation to the cubic perovskite structure, in which the c_p/a_p parameters ratio must be one [15]. In $Nd_{0.85}Gd_{0.15}AlO_3$ such transformation is predicted to occur at 2140 K (Fig. 7), which is somewhat higher than the average transition temperature reported in the literature for a "pure" $NdAlO_3$.

Based on the results of DTA measurements and *in situ* synchrotron powder diffraction examinations, as well as available literature data, the phase diagram of the pseudo-binary system $NdAlO_3$–$GdAlO_3$ has been constructed (Fig. 8). According to this diagram, three kinds of solid solutions with different types of perovskite structures exist in the $NdAlO_3$–$GdAlO_3$ system, depending on composition and temperature. Solid solutions $Nd_{1-x}Gd_xAlO_3$ with orthorhombic and rhombohedral perovskite structures exist in a wide temperature and concentration range, whereas a cubic perovskite phase is predicted to exist in the Nd-rich corner in a narrow temperature range between ~2100 K and the solidus line.

4. Discussion

Phase and structural behaviour in the $NdAlO_3$–$GdAlO_3$ pseudobinary system follows well the general trends observed in the related $NdAlO_3$–$RAlO_3$ [24, 31] and $RAlO_3$–$GdAlO_3$ [15, 32] systems, in which two kinds of the solid solutions are formed based on the rhombohedral and orthorhombic perovskite structures. Morphotropic transition between both kinds of perovskite structure takes place at ~0.27 [24], 0.18–0.25 [31], 0.15 (this work) and 0.08 [31] molar fraction x of R-component in the $(1-x)NdAlO_3$–$xRAlO_3$ systems with Sm, Eu, Gd and Dy, respectively. In the $(1-x)RAlO_3$–$xGdAlO_3$ series (R = La, Pr, Nd) the boundaries between rhombohedral and orthorhombic structures are located at x = 0.35–0.40 [15], x = 0.20–0.22 [32] and x = 0.15 (this work). Formation of metrically tetragonal and cubic structures observed in $Nd_{1-x}Gd_xAlO_3$ solid solution due to the lattice parameters crossover is also typical for the $RAlO_3$–$R'AlO_3$ systems, in which the end members possess different kinds of distorted perovskite structures, namely rhombohedral $R\bar{3}c$ and orthorhombic *Pbnm*. As it was shown in [15], an increase of the radius of R-cation in $RAlO_3$ and $R_{1-x}R'_xAlO_3$ series leads to increase of Goldschmidt tolerance factor t and consequently decrease of deformation of orthorhombic *Pbnm* perovskite structure, which is accompanied by increase of the a and c parameters and noticeable reduction of the b parameter. As a result, a lattice crossover occurs at certain compositions of orthorhombic solid solutions in the $LaAlO_3$–$RAlO_3$ (R = Sm, Eu, Gd, Tb) [15], $PrAlO_3$–$RAlO_3$ (R = Sm, Eu, Gd) [32 – 34] and $NdAlO_3$–$RAlO_3$ (R = Sm, Eu)

[15, 24, 35] systems. Further decrease of the deformation of perovskite structure caused by increasing *R*-cation radii leads to transition from orthorhombic to rhombohedral structure. A phase transition to the rhombohedral $R\bar{3}c$ structure in RBO_3 perovskites always occurs at the radii of *R*-cation, where the orthorhombic *Pbnm* phase shows a lattice parameters order $b < a$ [36]. In the $RCoO_3$ and $RNiO_3$ series such transitions occur at $r \cong 1.18–1.21$ Å [36], whereas in the $RAlO_3$ aluminates transition from *Pbnm* to $R\bar{3}c$ structure takes place at $r = 1.156$ Å [15]. Similar behaviour was also observed among mixed rare earth cobaltites in the $LaCoO_3–SmCoO_3$ system [37], and just recently, in the $LaCoO_3–LaRhO_3$ system [38]. A crossover of all three normalised cell parameters of $LaCo_{1-x}Rh_xO_3$ solid solution occurs at $x = 0.5$ resulting in a dimensionally cubic orthorhombic structure, which subsequently transforms into rhombohedral one at $0.1 < x < 0.2$. In latter system the increase of tolerance factor and hence decrease of perovskite structural deformation is caused by the decreasing radii of *B*-cation in octahedral sites due to the Rh–Co substitution.

The phenomena of the lattice crossover is also observed in those systems, in which the end members display different unit cell parameter order within the same orthorhombic *Pbnm* structure, such as $LaGaO_3–RGaO_3$ (*R* = Ce, Pr, Nd, Sm, Eu, Gd) [15, 39–42], $LaCrO_3–RCrO_3$ (*R* = Ce, Pr, Nd, Sm, Eu [43, 44], $RCoO_3–R'CoO_3$ (*R* = Pr, Nd; *R*' = Sm, Gd) [45–46], $LaCrO_3–CaTiO_3$ [47], $LaRuO_3–SrRuO_3$ [48] and $PrCoO_3–PrFeO_3$ [49].

The influence of the chemical pressure, caused by increasing radii of *R* cation, on the structural and phase behaviour in the $NdAlO_3–GdAlO_3$ system is similar to the temperature effect. Usually, increasing temperature leads to decrease of deformation of orthorhombic perovskite structure and to the further phase transformation to the rhombohedral structure. As it was shown in [15, 50], the cell parameter sequence $a_p > c_p > b_p$ ($a_p > c_p \cong b_p$) observed in the orthorhombic perovskites of $GdFeO_3$ type, can serve as an indicator of the forthcoming phase transition from the orthorhombic to the rhombohedral structure with the increasing temperature. It was entirely confirmed in the present study. As it is seen from Fig. 6, right before the temperature driven phase transition in $Nd_{1-x}Gd_xAlO_3$ the cell parameters of orthorhombic phase adopt the same sequence $a_p > c_p \cong b_p$. A similar sequence of the lattice parameters (see range I on Fig. 3) is also observed in the $NdAlO_3–GdAlO_3$ system at room temperature before the concentration induced transition to the rhombohedral structure.

Observed phenomena of the lattice crossover in the perovskite systems could have diverse practical applications. All orthorhombic perovskites with $GdFeO_3$ type of structure are ferroelastics and therefore they are characterized by a complex domain and twin structures [51]. Especially complex microstructure with extremely high density of twin and domain

walls is expected in those systems in which the dimensionally cubic perovskite-like structures occur. Since the transport, dielectric, optical and mechanical properties are strongly affected by microstructural parameters of materials [52], they can by effectively tuned by crystal and twin structure engineering.

Acknowledgements

The work was supported in parts by the Ukrainian Ministry of Education and Sciences (Project "Neos") and an ICDD Grant-in-aid program. *In situ* high-temperature diffraction measurements were carried out during beamtimes allocated to HASYLAB Projects II-20060043 and I-20110214. Especial gratitude is addressed to A. Berghäuser for his kind assistance in maintenance of equipments during the measurements. L. Vasylechko acknowledges the Max-Planck-Gesellschaft for a research fellowship.

References

[1] S.Y. Cho, I.T. Kim, K.S. Hong, J. Mater. Res. 14 (1999) 114–119.

[2] S.Y. Cho, K.S. Hong, K.H. Ko, Mater. Res. Bull. 34 (1999) 511–516.

[3] B. Jancar, M. Valant, D. Suvorov, Chem. Mater. 16 (2004) 1075–1082.

[4] A. Sinha, B.P. Sharma, P. Gopalan, Electrochimica Acta, 51 (2006) 1184–1193.

[5] S.D. Han, S.P. Khatkar, V.B. Taxak, D. Kumar, J.-Y. Park, Mater. Sci. Eng. B 127 (2006) 272–275.

[6] H.H.S. Oliveira, M.A. Cebim, A.A. Da Silva, M.R. Davolos, J. Alloys Compd. 488 (2009) 619–623.

[7] Y. Liu, X. Tong, F. Lai, X. Chen, W. You, Physica B, 406 (2011) 1272–1275.

[8] G.S.R. Raju, J.Y. Park, H.C. Jung, B.K. Moon, J.H. Jeong, J.H. Kim, Curr. Appl. Phys. 9 (2009) e91–e95.

[9] J.W.M. Verweij, M.Th. Cohen-Adad, D. Bouttet, H. Lautesse, B. Moine, C. Pedrini, Chem. Phys. Lett. 239 (1995) 51–55.

[10] L.M. Qiu, T. Numaxawa, G. Thummes, Cryogenics 41 (2001) 693–696.

[11] Y. Waku, Adv. Mater. 10 (1998) 615–617.

[12] H. Su, J. Zhang, J. Yu, L. Liu, H. Fu, J. Alloys Compd. 509 (2011) 4420–4425.

[13] N. Nakagawa, H. Ohtsubo, A. Mitani, K. Shimizu, Y. Waku, J. Eur. Cer. Soc. 25 (2005) 1251–1257.

[14] G. Suresh, G. Seenivasan, M.V. Krishnaiah, P.S. Murti, J. Nucl. Mater. 249 (1997) 259–261.

[15] L. Vasylechko, A. Senyshyn, U. Bismayer, in: K.A. Gschneidner, Jr., J.-C.G. Bünzli and V.K. Pecharsky, Eds. Handbook on the Physics and Chemistry of Rare Earths, Vol. 39, North-Holland, Netherlands 2009, p.p. 113–295.

[16] S. Geller, V.B. Bala, Acta Crystallogr. 9 (1956) 1019–1025.

[17] J.F. Scott, Phys. Rev. 183 (1969) 823–825.

[18] M. Mizuno, T. Yamada, T. Noguchi, Yogio Kyokaishi (J. Ceram. Soc. Jpn.) 85 (1977) 543–548.

[19] J. Coutures, J.P. Coutures, J. Solid State Chem. 52 (1984) 95–100.

[20] S. Geller, P.M. Raccah, Phys. Rev. B 2 (1970) 1167–1172.

[21] C.J. Howard, B. J. Kennedy, B.C. Chakoumakos, J. Phys.: Condens. Matter. 12 (2000) 349–365.

[22] R. Mazelsky, W.E. Kramer, R.H. Hopkins, J. Cryst. Growth 2 (1968) 209–214.

[23] K.I. Portnoj, N.I. Timofeeva, Oxygen Compounds of Rare Earth Element, Metallurgia, Moskow, 1986 (*in Russian*).

[24] A. Yoshikawa, A. Saitow, H. Horiuchi, T. Shishido, T. Fukuda, J. Alloys Compd. 266 (1998) 104–110.

[25] L. Vasylechko, A. Senyshyn, D. Trots, R. Niewa, W. Schnelle, M. Knapp, J. Solid State Chem. 180 (2007) 1277–1290.

[26] E. Palacios, J. Bartolome, F. Luis, Phys. Rev. B 68 (2003) 224425–10.

[27] M. Knapp, V. Joco, C. Baehtz, H.H. Brecht, A. Berghaeuser, H. Ehrenberg, H. von Seggern, H. Fuess, Nucl. Instrum. Methods A 521 (2004) 565–570.

[28] M. C. Baehtz, H. Ehrenberg, H. Fuess, J. Synchrotron Rad. 11 (2004) 328–334.

[29] L.G. Akselrud, P.Yu. Zavalij, Yu. Grin, V.K. Pecharsky, B. Baumgartner, E. Wölfel, Mater. Sci. Forum 133-136 (1993) 335–342.

[30] R.D. Shannon, Acta Crystallogr. A32 (1976) 751–757.

[31] H. Brusset, M.H. Gillier-Pandraud, M.C. Saine, Mater. Res. Bull. 10 (1975) 481–488.

[32] T. Basyuk, L. Vasylechko, S. Fadeev, V. Berezovets, D. Trots, R. Niewa, Acta Phys. Pol. A 117 (2010) 98–103.

[33] T.V. Basyuk, L.O. Vasylechko, I.I. Syvorotka, V. Berezovets, S.V. Fadeev, Visnyk Lviv Polytechnic Natl. University. Electronics 646 (2009) 3–10 (in Ukrainian).

[34] T. Basyuk, V. Berezovets, D. Trots, S. Hoffmann, R. Niewa, L. Vasylechko, Z. Kristallogr. Proc. 1 (2011) 319–324.

[35] N. Ohon, N. Ivashkiv, S. Hoffmann, L. Vasylechko, in: Proceedings of the International Conference on Oxide Materials for Electronic Engineering – fabrication, properties and applications (OMEE-2012). Lviv, Ukraine, September 3–7, 2012. P.120–121.

[36] J.-S. Zhou, J.B. Goodenough, Phys. Rev. Lett. 94 (2005) 065501–4.

[37] Y. Sadaoka, E. Traversa, M. Sakamoto, J. Mater. Chem. 6 (1996) 1355–1360.

[38] J. Li, A.E. Smith, K.-S. Kwong, C. Powell, A.W. Sleight, M.A. Subramanian, J. Solid State Chem. 183 (2010) 1388–1393.

[39] L. Vasylechko, A. Matkovski, A. Suchocki, D. Savytskii, I. Syvorotka, J. Alloys Compd. 286 (1999) 213–218.

[40] L. Vasylechko, M. Berkowski, A. Matkovskii, W. Piekarczyk, D. Savytskii, J. Alloys Compd. 300-301 (2000) 471–474.

[41] M. Berkowski, J. Fink-Finowicki, P. Byszewski, R. Diduszko, E. Kowalska, R. Aleksijko, W. Piekarczyk, L.O. Vasylechko, D.I. Savytskij, L. Perchuć, J. Kapuśniak, J. Crystal Growth 222 (2001) 194–201.

[42] L. Vasylechko, R. Niewa, H. Borrmann, M. Knapp, D. Savytskii, A. Matkovski, U. Bismayer, M. Berkowski, Solid State Ionics 143 (2001) 219–227.

[43] R. Shukla, J. Manjanna, A.K. Bera, S.M. Yusuf, A.K. Tyagi, Inorg. Chem. 48 (2009) 11691–11696.

[44] L. Vasylechko, T. Basyuk, V. Vashook, S. Hoffmann, D. Trots, HASYLAB Ann. Rep. (2010). *http://hasylab.desy.de/annual_report/files/2010/20101175.pdf*

[45] S.V. Kurgan, G.S. Petrov, L.A. Bashkirov, A.I. Klyndyuk, Inorg. Mater. 40 (2004) 1224–1228.

[46] L. Vasylechko, O. Myakush, Yu. Prots, A. Senyshyn, HASYLAB Ann. Rep. (2010). http://hasylab.desy.de/annual_report/files/2010/20101085.pdf

[47] V. Vashook, L. Vasylechko, N. Trofimenko, M. Kuznecov, P. Otchik, J. Zosel, U. Guth, J. Alloys Compd. 419 (2006) 271–280.

[48] R.J. Bouchard, J.F. Weiher, J. Solid State Chem. 4 (1972) 80–86.

[49] O. Kharko, L. Vasylechko, Visnyk Lviv Polytechnic Natl. University. Electronics 734 (2012) 119-126 (in Ukrainian).

[50] L. Vasylechko, Ye. Pivak, A. Senyshyn, D. Savytskii, M. Berkowski, H. Borrmann, M. Knapp, C. Paulmann, J. Solid State Chem. 178 (2005) 270–278.

[51] D. Savytskii, T. Tataryn, U. Bismayer, Acta Phys. Pol. A 117 (2010) 78–85.

[52] G. Catalan, J. Seidel, R. Ramesh, J. F. Scott, Rev. Mod. Phys. 84 (2012) 119–156.

Figures:

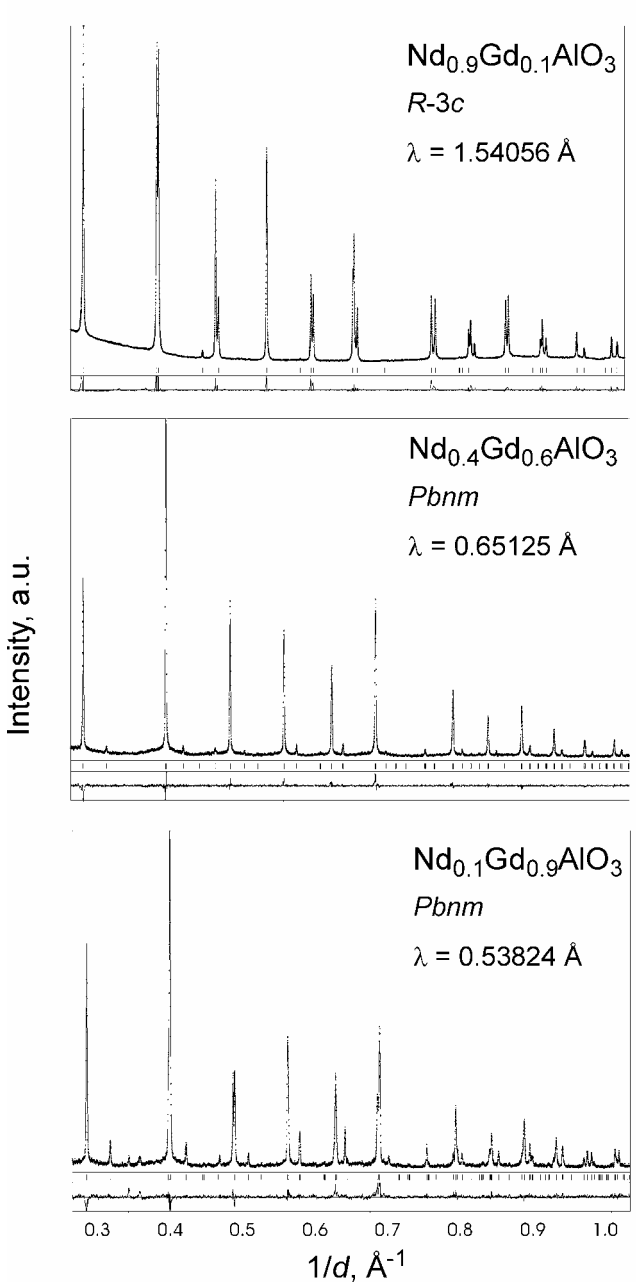

Fig. 1. Laboratory X-ray (top) and synchrotron (middle, bottom) powder diffraction patterns of $Nd_{0.9}Gd_{0.1}AlO_3$, $Nd_{0.4}Gd_{0.6}AlO_3$ and $Nd_{0.1}Gd_{0.9}AlO_3$ recorded at room temperature (dots) in comparison with the calculated patterns. The difference between measured and calculated profiles is shown as a curve below the diagrams, reflection positions are indicated by ticks.

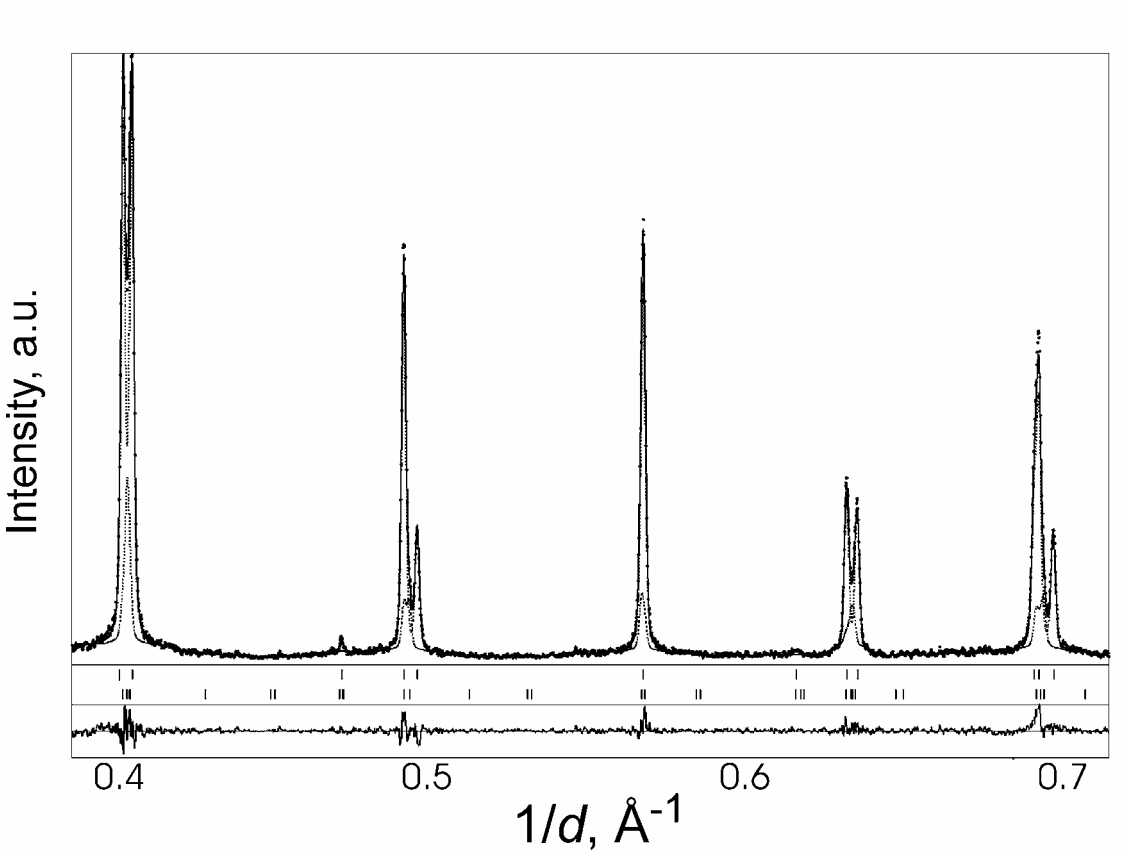

Fig. 2. Graphical results of two-phase Rietveld refinement showing coexistence of rhombohedral $R\bar{3}c$ (83 wt.%) and orthorhombic *Pbnm* (17 wt.%) perovskite phases in the $Nd_{0.85}Gd_{0.15}AlO_3$ sample at room temperature. Cutout of the experimental X-ray synchrotron powder diffraction pattern (λ = 0.53824 Å) is shown in comparison with the calculated patterns. The difference between measured and calculated profiles is shown as a curve below the diagrams. Short vertical bars indicate the positions of diffraction maxima of $R\bar{3}c$ and *Pbnm* phases (upper and lower rows, respectively).

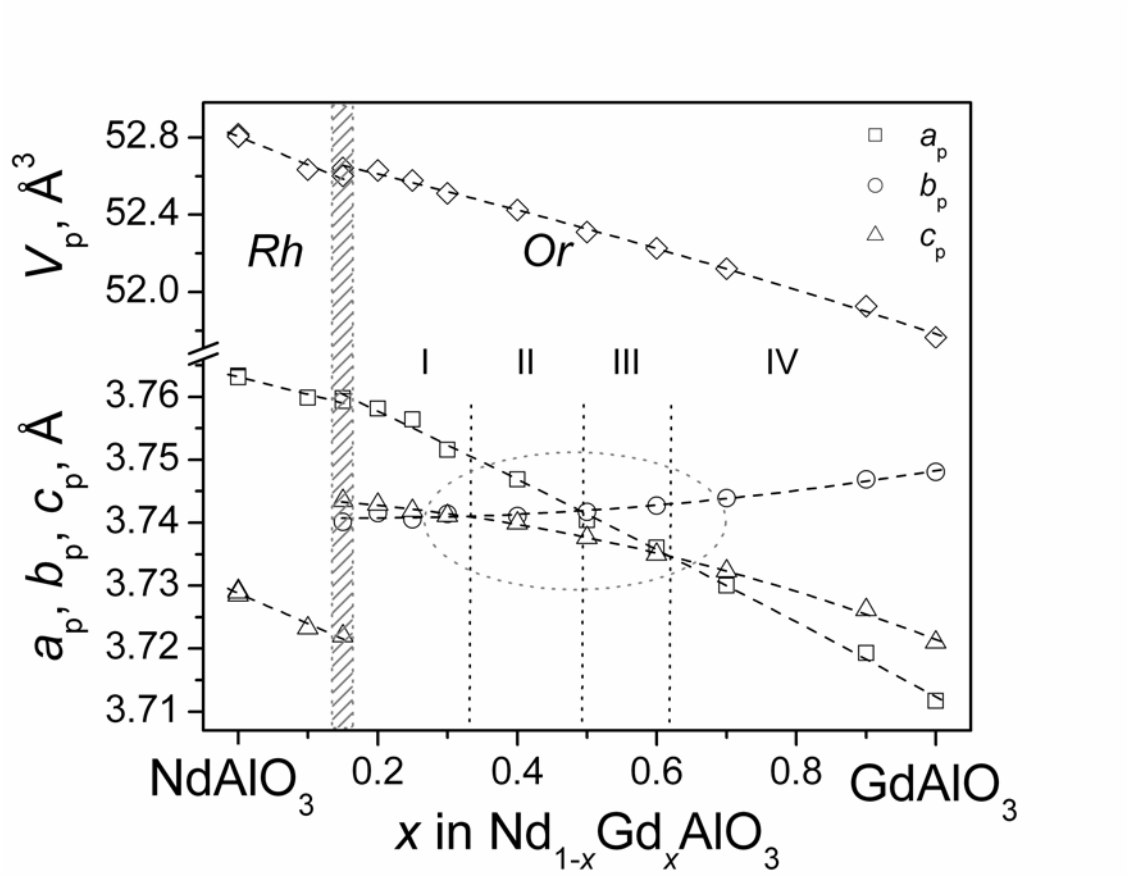

Fig. 3. Concentration dependencies of normalized lattice parameters and unit cell volumes of $Nd_{1-x}Gd_xAlO_3$ solid solutions at room temperature. Cell dimensions of $NdAlO_3$ and $GdAlO_3$ are taken from ref. [16]. Here and in the Fig. 6 the error bars (typically $\pm(1\text{-}2)\times10^{-4}$ Å) are smaller than the symbols in the graph. Lattice parameters and volumes of the rhombohedral (*Rh*) and orthorhombic (*Or*) cells are normalized to the perovskite (*P*) ones as follows: $a_p = a_r/\sqrt{2}$, $c_p = c_r/\sqrt{12}$, $V_p = V_r/6$; $a_p = a_o/\sqrt{2}$, $b_p = b_o/\sqrt{2}$, $c_p = c_o/2$, $V_p = V_o/4$. The dashed lines are polynomials fits for guides for eye. The hatched area shows two-phase perovskite region.

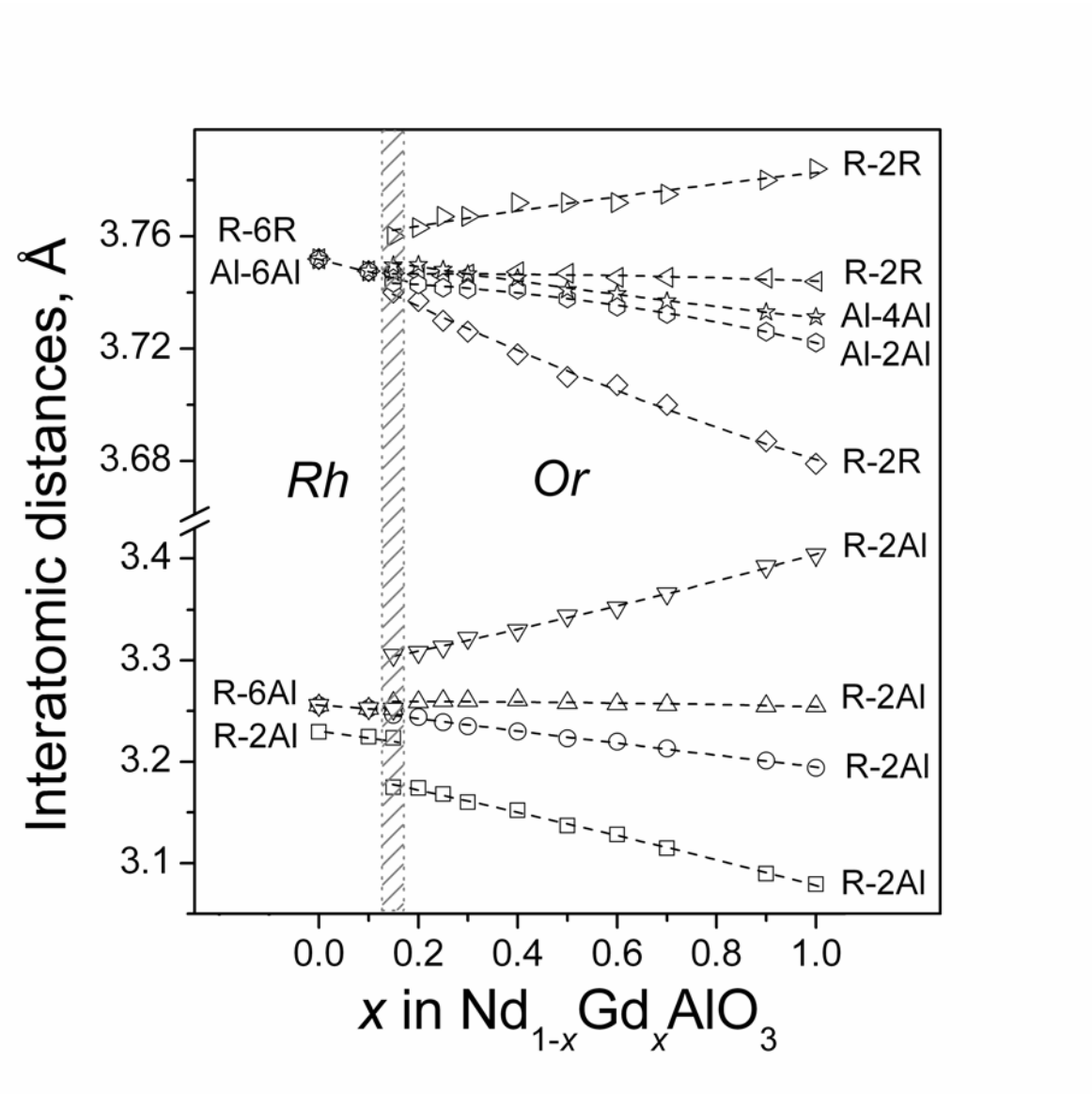

Fig. 4. Concentration dependencies of the interatomic distances R-Al, R-R (R = $Nd_{1-x}Gd_x$) and Al-Al in $Nd_{1-x}Gd_xAlO_3$ solid solutions at room temperature. The dashed lines are polynomials fits for guides for eye. The hatched area shows two-phase perovskite region.

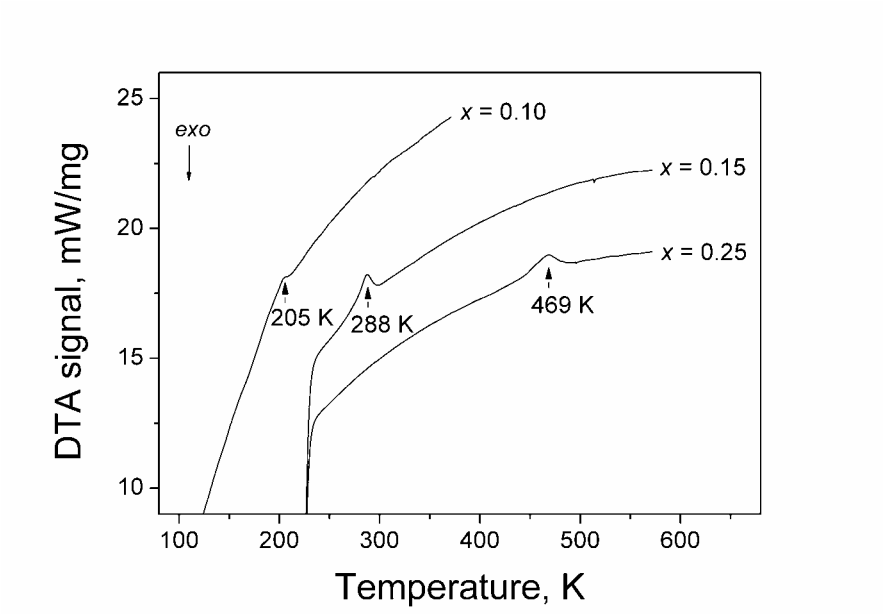

Fig. 5. DTA curves representing first-order phase transition in $Nd_{1-x}Gd_xAlO_3$ for x = 0.10, 0.15 and 0.25.

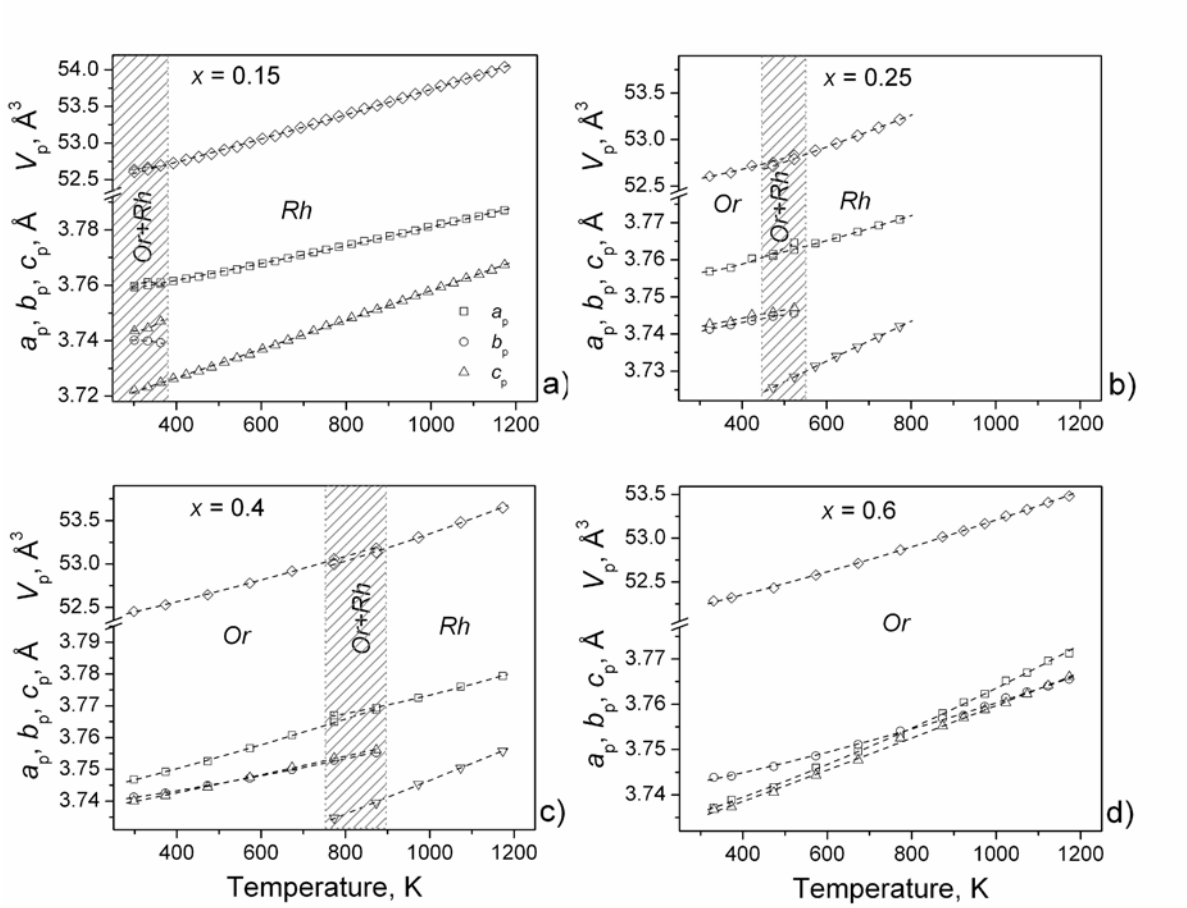

Fig. 6. Temperature dependencies of normalized lattice parameters and cell volumes (definition see Fig. 3) of $Nd_{1-x}Gd_xAlO_3$. The dashed lines are polynomials fits for guides for eye. The hatched areas show two-phase perovskite region.

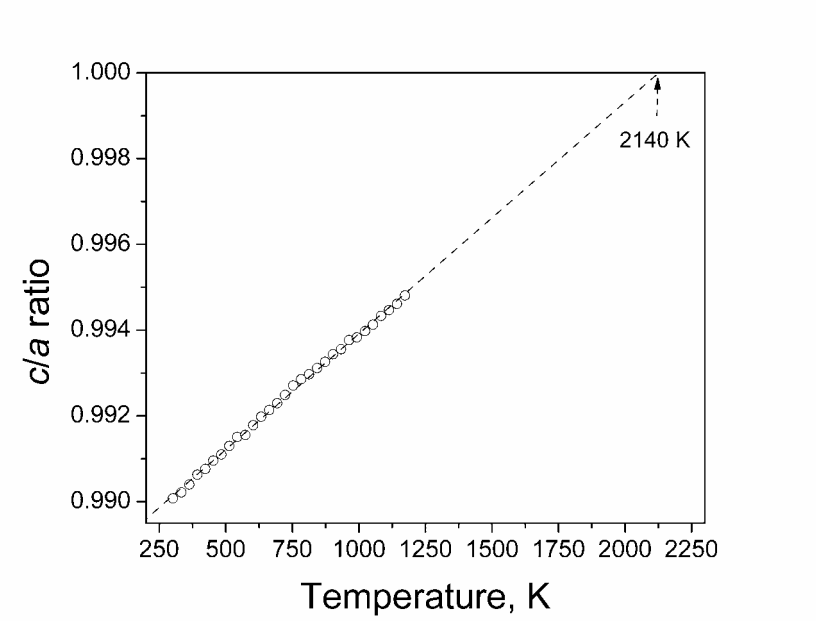

Fig. 7. The ratio of normalized lattice parameters of rhombohedral phase of $Nd_{0.85}Gd_{0.15}AlO_3$ in the temperature range of 298–1173 K and extrapolation to the expected phase transition to the cubic structure.

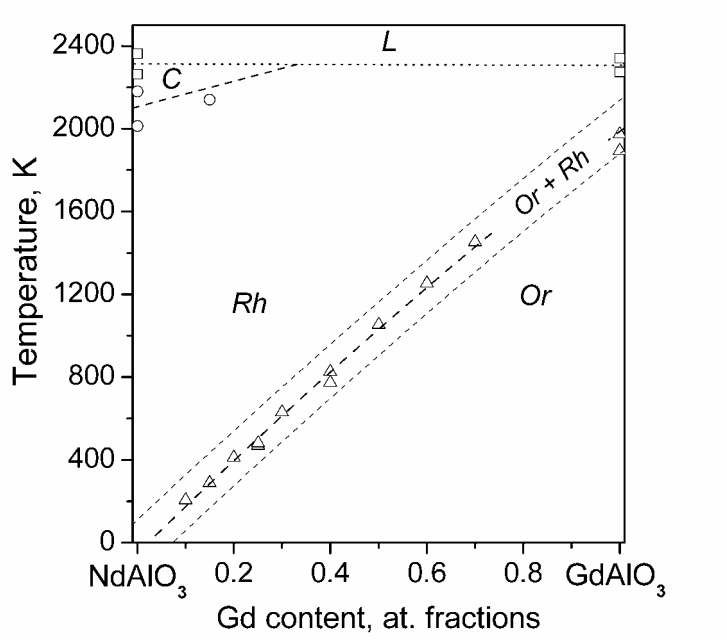

Fig. 8. Phase diagram of the pseudo-binary system $NdAlO_3$–$GdAlO_3$. The letters *L*, *C*, *Rh*, and *Or* designate liquid, cubic, rhombohedral and orthorhombic phase fields, respectively. Transition temperatures and melting points for $NdAlO_3$ and $GdAlO_3$ are taken from the literature [16–26]. The symbols indicate the temperatures of phase transitions $Pbnm$–$R\bar{3}c$ (triangles), $R\bar{3}c$–$Pm\bar{3}m$ (circles) and melting points (squares).

Table 1. Lattice parameters, positional and displacement parameters of atoms in $Nd_{1-x}Gd_xAlO_3$ at RT

Atoms, sites	Parameters	x in $Nd_{1-x}Gd_xAlO_3$, space groups										
		0.1	0.15		0.2	0.25	0.3	0.4	0.5	0.6	0.7	0.9
		$R\bar{3}c$	$R\bar{3}c$	*Pbnm*	*Pbnm*	*Pbnm*	*Pbnm*	*Pbnm*	*Pbnm*	*Pbnm*	*Pbnm*	*Pbnm*
	a, Å	5.31670(5)	5.3165(1)	5.3167(6)	5.3148(2)	5.3109(2)	5.3054(2)	5.2995(1)	5.2891(4)	5.2836(3)	5.2749(2)	5.2598(1)
	b, Å	-	-	5.2890(5)	5.2913(2)	5.2904(2)	5.2911(2)	5.2918(1)	5.2918(3)	5.2930(2)	5.2947(2)	5.2988(1)
	c, Å	12.8991(2)	12.8936(3)	7.4870(8)	7.4858(3)	7.4838(2)	7.4824(3)	7.4817(2)	7.4758(5)	7.4700(4)	7.4647(3)	7.4523(2)
Nd(Gd), 6*a* in $R\bar{3}c$ 4*c* in *Pbnm*	x	0	0	-0.0013(9)	-0.0018(9)	-0.0025(8)	-0.0028(9)	-0.0036(4)	-0.0041(7)	-0.0043(7)	-0.0050(6)	-0.0063(4)
	y	0	0	0.0150(3)	0.0155(3)	0.0168(2)	0.0187(2)	0.0205(1)	0.0239(3)	0.0259(3)	0.0291(2)	0.0349(2)
	z	¼	¼	¼	¼	¼	¼	¼	¼	¼	¼	¼
	B_{iso}, Å^2	0.58(2)	0.76(2)	0.76(2)	0.79(2)	0.86(3)	0.79(2)	0.91(1)	0.86(3)	0.81(3)	0.89(2)	0.86(1)
Al, 6*b* in $R\bar{3}c$ 4*b* in *Pbnm*	x	0	0	0	0	0	0	0	0	0	0	0
	y	0	0	½	½	½	½	½	½	½	½	½
	z	0	0	0	0	0	0	0	0	0	0	0
	B_{iso}, Å^2	1.07(6)	0.46(6)	0.49(8)	0.43(9)	0.65(11)	0.55(9)	0.78(4)	0.55(10)	0.47(11)	0.69(10)	0.72(7)
O1, 18*e* in $R\bar{3}c$ 4*c* in *Pbnm*	x	0.5471(8)	0.5509(11)	0.065(5)	0.064(5)	0.064(5)	0.063(6)	0.078(4)	0.065(8)	0.072(7)	0.072(6)	0.079(3)
	y	0	0	0.510(4)	0.507(4)	0.509(4)	0.486(4)	0.494(2)	0.501(4)	0.487(4)	0.472(4)	0.485(3)
	z	¼	¼	¼	¼	¼	¼	¼	¼	¼	¼	¼
	B_{iso}, Å^2	1.64(10)	0.96(12)	1.0(5)	0.6(6)	0.9(7)	0.5(7)	0.8(3)	0.6(13)	0.4(9)	0.8(6)	0.8(3)
O2, 8*d* in *Pbnm*	x	-	-	-0.270(5)	-0.269(6)	-0.276(4)	-0.281(5)	-0.275(3)	-0.273(6)	-0.275(5)	-0.268(5)	-0.267(3)
	y	-	-	0.278(5)	0.278(5)	0.246(5)	0.286(5)	0.277(3)	0.285(5)	0.271(5)	0.280(4)	0.293(2)
	z	-	-	0.030(3)	0.034(3)	0.037(3)	0.024(3)	0.027(2)	0.038(4)	0.041(4)	0.035(3)	0.034(2)
	B_{iso}, Å^2	-	-	1.0(4)	1.0(4)	1.4(5)	1.0(4)	0.8(2)	0.7(6)	1.6(6)	0.9(4)	1.0(2)
R_I		0.077	0.067	0.284	0.094	0.101	0.085	0.092	0.077	0.092	0.095	0.090
R_P		0.097	0.113	0.113	0.136	0.165	0.116	0.117	0.125	0.149	0.159	0.138